Article

# Flexible and Freestanding MoS$_2$/Graphene Composite for High-Performance Supercapacitors

Chandra Sekhar Bongu, Mohan Raj Krishnan, Abdelrahman Soliman, Muhammad Arsalan, and Edreese H. Alsharaeh*
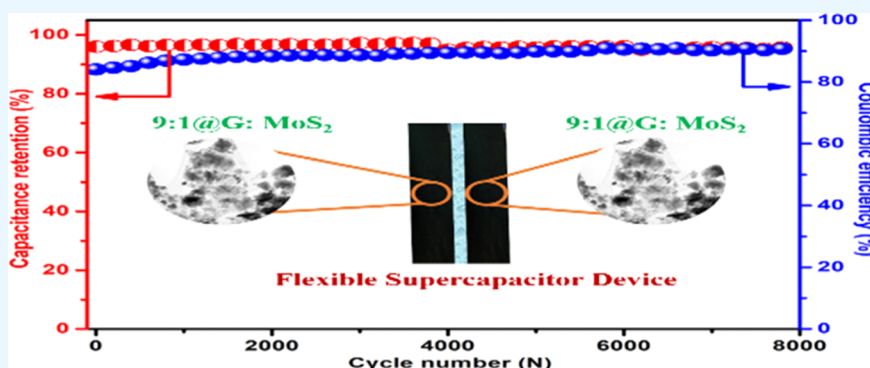
Cite This: ACS Omega 2023, 8, 36789−36800

Read Online

| ACCESS | Metrics & More | Article Recommendations | Supporting Information |

**ABSTRACT:** Two-dimensional atomically thick materials such as graphene and layered molybdenum disulfide (MoS$_2$) have been studied as potential energy storage materials because of their high specific surface area, potential redox activity, and mechanical flexibility. However, because of the layered structure restacking and poor electrical conductivity, these materials are unable to attain their full potential. Composite electrodes made of a mixture of graphene and MoS$_2$ have been shown to partially resolve these issues in the past, although their performance is still limited by inadequate mixing at the nanoscale. Herein, we report three composites via a simple ball-milling method and analyze supercapacitor electrodes. Compared with pristine graphene and MoS$_2$, the composites showed high capacitance. The as-obtained MoS$_2$@Graphene composite (1:9) possesses a high surface area and uniform dispersion of MoS$_2$ on the graphene sheet. The MoS$_2$@Graphene (1:9) composite electrode has a high specific capacitance of 248 F g$^{-1}$ at 5 A g$^{-1}$ in an electrochemical supercapacitor compared with the other two composites. Simultaneously, the flexible symmetric supercapacitor device prepared demonstrated superior flexibility and a long lifespan (93% capacitance retention after 8000 cycles) with no obvious changes in performance under different angles. In portable and wearable energy storage devices, the current experimental results will result in scalable, freestanding hybrid electrodes with improved, flexible, supercapacitive performance.

## 1. INTRODUCTION

The need for developing clean, renewable, and sustainable alternative sources of energy is driven by the ever-growing environmental risks brought on by increased pollution and the overuse of the present traditional sources of energy. In addition, the creation of effective, miniature, and flexible technologies that may help overcome the existing limitations is required due to the increasing reliance of society on technology. The intermittent nature of renewable energy sources that are now accessible makes their integration into effective energy storage systems necessary in order to put them to use. Batteries and capacitors are two energy storage devices that are most frequently employed, and both have their individual advantages and disadvantages.[1] However, the battery has a high energy density and the capacitor has a high power density. Supercapacitors can easily fill out the gap between redox chemical batteries and traditional capacitors. Supercapacitors also have a long lifespan, are lightweight,

charge and discharge quickly, and are environmentally friendly.[2] Because of these benefits, supercapacitors are anticipated to successfully replace current energy storage technologies.

SCs can be divided into electrical double-layer capacitors (EDLCs) and pseudocapacitors based on the energy storage mechanism.[3] While pseudocapacitors primarily use electro-active conducting polymers or transition metal oxides as electrode materials, EDLCs typically consist of carbon materials or carbon-based hybrid materials with high surface

areas and acceptable pore sizes.[4] Because of their excellent electrochemical capacitive properties, broad potential range, low cost, environmental friendliness, and distinctive structure—property relationships, 2D transition metal dichalcogenides, such as molybdenum disulfide ($MoS_2$), tungsten disulfide, and vanadium disulfide, have drawn increasing interest in energy storage, particularly in flexible supercapacitors (FSCs).[5−7] Because of its distinct physical and chemical characteristics, molybdenum disulfide ($MoS_2$), a typical transition metal sulfide, has received a lot of attention.[8,9] However, due to the interlayer van der Waals interactions and high surface energy, $MoS_2$ has poor electronic conductivity and undergoes significant volume change throughout the charge/discharge process.[10,11] Eventually, the cycling abilities of SCs substantially deteriorate.

To improve the electrochemical performance of $MoS_2$ and, to some part, overcome the aforementioned obstacles, many researchers coat $MoS_2$ onto a conductive network to create a hierarchical porous network. $MoS_2$ is grown on top of conductive scaffolds, such as carbon nanotubes,[12] polyanilines,[13] carbon nanofibers,[14] and mesoporous carbon,[15] to improve the electrode conductivity and limit volume change. Graphene is regarded as a promising candidate material among these alternative network scaffolds due to its large surface area, high electrical conductivity, and exceptional mechanical capabilities.[16−18]

It is imperative to develop flexible and high-performance energy storage devices as a power supply, given the increasing development of wearable electronics.[1−5] Flexible fiber supercapacitors (FSCs), which have high flexibility, low weight, and the ability to be woven into fabrics, are gaining popularity as smart energy sources for wearable devices. FSCs made of various electroactive materials have been created in recent years and have demonstrated remarkable electrochemical performance when they are used to power wearable electronics with a variety of applications. Because of its low weight, low volume, excellent conductivity, high mechanical strength, and knittability, graphene, in particular, has been seen as an appealing electrode material for FSCs. Among them, flexible all-solid-state supercapacitors based on polymer gel electrolytes have the characteristics of a simple assembly process and excellent mechanical strength, which can meet the needs of more application scenarios and become the main focus in the field of flexible energy storage devices in the near future.[6−9] Among various polymers that have been explored for the preparation of polymer gel electrolytes, poly(vinyl alcohol) (PVA) is shown to be advantageous because of its hydrophilicity, polarity, high mechanical characteristics, easy processability to form a thin film, and noncorrosive nature.[19,20] In addition, PVA is a nontoxic, cheap, and biodegradable polymer in comparison to other synthetic polymeric candidates.[21] The addition of salt (KOH) into the PVA host gel results in the formation of free ions that can eventually interact with the polar groups of PVA. Consequently, the structural arrangement of the PVA host gel is sufficiently altered to allow ionic movement within the PVA.[19,22]

In the present study, we designed and fabricated a $MoS_2$/graphene composite electrode by a ball-milling method and utilized it directly as an electrode for SCs. Further, an electrochemical study was carried out by a symmetric device where the composite ($MoS_2$/graphene, 1:9) was used as a freestanding electrode and PVA-KOH as the solid electrolyte. At a current density of 5 A g$^{-1}$, the $MoS_2$/graphene (1:9)

electrode exhibited outstanding specific capacitance and a capacitance retention of 97.3% after 8000 cycles. The better electrochemical performance of the $MoS_2$/graphene (1:9) composite electrode points toward its enormous application potential in energy storage for small, light, and flexible electronic devices.

## 2. EXPERIMENTAL SECTION

**2.1. Materials.** Graphene nanoplates (XG Sciences Inc., Graphene-M-25; Grade M; particles have an average thickness of approximately 6−8 nm; surface area: 120−150 m$^2$/g; average particle diameter: 25 $\mu$m), $MoS_2$ (Graphene Supermarket Inc.; purity: 99.0%; average particle size: ∼ 90 nm; specific surface area: ∼35 m$^2$/g; morphology: nearly spherical; bulk density: ∼0.78 g/cm$^3$; true density: 5.06 g/cm$^3$), poly(vinyl alcohol) (PVA) (Loba Chemie; hydrolysis: 98−99 mol %; degree of polymerization: 1700−1800), and potassium hydroxide pellets (KOH; Loba Chemie; purity: 85.0%) were procured. All reagents were used as received.

**2.2. Synthesis of the $MoS_2$/Graphene Composite.** $MoS_2$/graphene composites (50:50, 10:90, and 90:10) were synthesized via the sonication and ball-milling process using graphene nanoplates and $MoS_2$ as the starting materials. First, graphene nanoplates were ultrasonically dispersed for 1 h in ethanol, and $MoS_2$ was added to the above solution and subjected to continuous sonication for 1 h to obtain a uniform dispersion. The $MoS_2$@graphene nanohybrid obtained was dried in a vacuum furnace at 100 °C for 6 h. Afterward, $MoS_2$ with graphene composites (50:50, 10:90, and 90:10 ratios) was ground for 30 min and subsequently ball-milled with a SPEX samplePrep P instrument model number 8000 M MIXER/MILL using two different sizes of balls (four balls with 6.3 mm and two balls with 12.5 mm prepared with stainless steel), and the powder weight ratio of balls to material was 4:1 with a rotational speed (rpm) of 1060 for 45 min to obtain better uniformity.

**2.3. Polymer Gel Electrolyte Preparation.** Preparation of the gel electrolyte for freestanding supercapacitor application. First, 15% of the poly(vinyl alcohol) (PVA) solution was prepared by adding 15 g of PVA to 85 g of hot DI water (preheated to 80 °C) under vigorous stirring. The stirring continued until a clear solution was obtained. To the PVA solution, 6 M KOH solution was added dropwise while increasing the temperature to 90 °C under constant stirring. The solution was cooled to obtain the PVA-KOH gel. The PVA-KOH gel electrolyte film was obtained by solution casting of the above gel. To prepare films with a specific thickness, we drew the films using doctor blades.

## 3. CHARACTERIZATION

**3.1. Physical characterization.** A Bruker D8 Advance X-ray diffractometer with a $2\theta$ scanning range of 10−70° and CuKa radiation ($l$ = 1.5406) was used to acquire the XRD data. At room temperature, Raman spectra were collected using WITec Apyron Raman microscope equipment and a 532 nm solid-state laser as the excitation source. To study the surface morphology, the presence of carbon coating was determined and energy-dispersive spectroscopy (EDS) and transmission electron microscopy (TEM, Tecnai 20 G2 (FEI)) were performed. The surface area and the pore size of the samples were determined by the Brunauer−Emmett−Teller (BET)

method by nitrogen adsorption/desorption using Quantachrome, NOVA version 11.02.

**3.2. Electrochemical Measurements.** Using a BioLogic SP-300 Modular electrochemical workstation, the electrochemical characteristics of the samples were examined at room temperature by galvanostatic charge/discharge (GCD) tests, cyclic voltammetry (CV), and electrochemical impedance spectroscopy (EIS). In a three-electrode cell with 6 M KOH as the electrolyte and platinum foil and Ag/AgCl as the counter and reference electrodes, respectively, electrochemical tests of the individual electrodes were carried out. The $MoS_2$/graphene nanocomposites (1:9. 5:5, and 9:1), along with carbon black (Super-P) and PVDF, were combined to create the working electrode in the weight ratio of 80:10:10. The paste was ground using N-methyl-2-pyrrolidone as the solvent and then applied to a nickel mesh current collector to prepare the electrode. After drying overnight in a vacuum oven at 60 °C, the functional electrodes were acquired. The mass loading on the nickel foam in the three-electrode system is 2.0 mg. CV and CD studies were conducted at various scan speeds ranging from 10 to 500 mV s$^{-1}$, respectively, in the potential window of −0.6−0.4 V (vs Ag/AgCl).

*3.2.1. Assembly of Coin Cell SCs.* In order to study the potential application of these electrode materials in a supercapacitor, the electrode materials were investigated in a two-electrode configuration. For the device application, the above-prepared electrode slurry was coated on an Al foil and dried in a vacuum oven overnight at 70 °C. The electrode was cut into circular disks of 15 mm diameter and dipped into 6 M KOH to obtain the freestanding electrode. Using two freestanding electrodes and Whatman filter paper as a separator, the coin cell device was fabricated for the electrochemical study.

*3.2.2. Synthesis of an All-Solid-State Flexible Symmetric Supercapacitor.* The flexible symmetric supercapacitor was fabricated using $MoS_2$/graphene (1:9) as an electrode. The PVA-KOH gel electrolyte was sandwiched between two identical pieces of the $MoS_2$/graphene (1:9) electrode to obtain the flexible device.

All measurements were performed at room temperature. The capacitance with respect to the single electrode was calculated using the charge integrated from GCD curves, according to the following formula.[23−27]

$$C_s, g = \frac{I\Delta t_d}{m\Delta V} \quad (1)$$

where $C_s$ (F g$^{-1}$) is the specific capacitance of the material, $I$ (A) is the current, $\Delta$ (s) is the discharge time, $m$ (g) is the active mass of the electrode, and $\Delta V$ (V) is the working potential window.

The energy density ($E$) and power density ($P$) of the supercapacitor cell were estimated according to eqs 2 and 3, respectively, represented as follows

$$E = \frac{0.5C_{CD}(V_f - V_i)^2}{3.6} \quad (2)$$

$$P = \frac{3600E}{\Delta t} \quad (3)$$

where $C_{CD}$ (F/g) signifies the specific capacitance, $(V_f - V_i)$ (V) represents the potential window, and $\Delta t$ is the discharge time from the charge/discharge curve in the case of the device.

## 4. RESULTS AND DISCUSSION

The as-prepared electrode materials were examined by X-ray diffraction (XRD) in the range of 5° to 70° to determine the crystalline structure and overall crystallinity, as shown in Figure 1. The diffraction peaks of pristine graphene (black color)
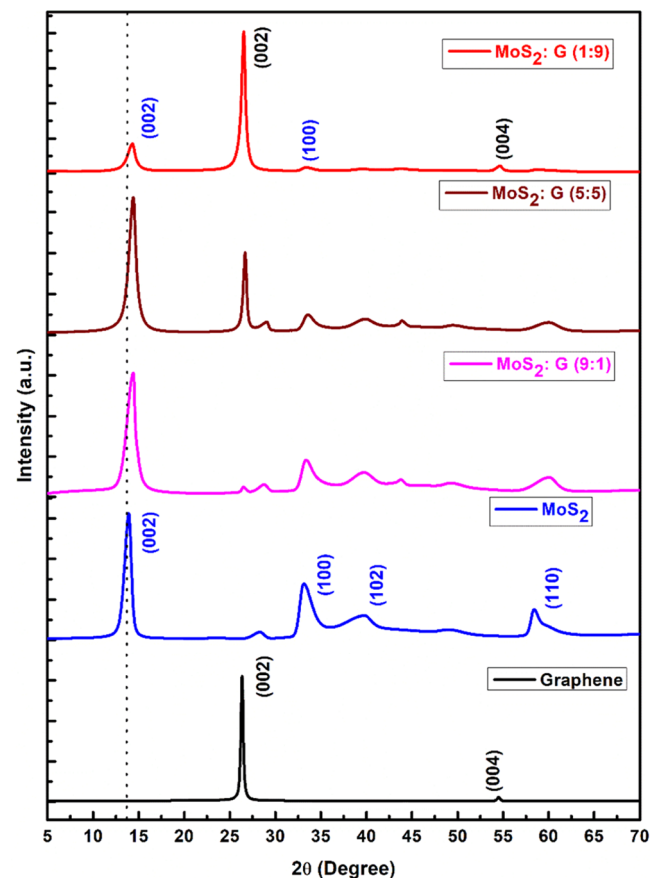


**Figure 1.** X-ray diffraction patterns of pristine graphene, $MoS_2$, and $MoS_2$:G (9:1, 5:5, and 1:9) composites.

appear at $2\theta$ = 26 and 54°, which correspond to the (002) and (004) planes, respectively. The diffraction pattern of the pure $MoS_2$ sample matches well with the JCPDS 37-1492 reported structure of 2H-$MoS_2$, and diffraction peaks appear at $2\theta$ = 13.9, 33.2, 40.1, and 58.3°, which correspond to the (002), (100), (103), and (004) planes, respectively. Notably, $MoS_2$/graphene composites show the presence of sharp and strong peaks, confirming the crystallinity of the final product obtained. The presence of the (002) peak at roughly 26.5°, which represents the graphene interlayer spacing, implies that the composites were mixed uniformly.[28] Compared to the bulk $MoS_2$, the observed diffraction patterns had a slightly higher diffraction angle shift, which indicates the presence of layers of $MoS_2$ that are stacked randomly. This may be because graphene was intercalated between the layers during synthesis. In addition, the (002) peak in the $MoS_2$/graphene (1:9) composition displays low intensity, which means that the composite shows higher interlayer expansion than the remaining two composites.[8,28]

A trustworthy diagnostic method for confirming the $MoS_2$ and carbon components is Raman spectroscopy. Figure 2 displays the room-temperature Raman spectra of the $MoS_2$/graphene composites, pristine graphene, and $MoS_2$ (Figures S1
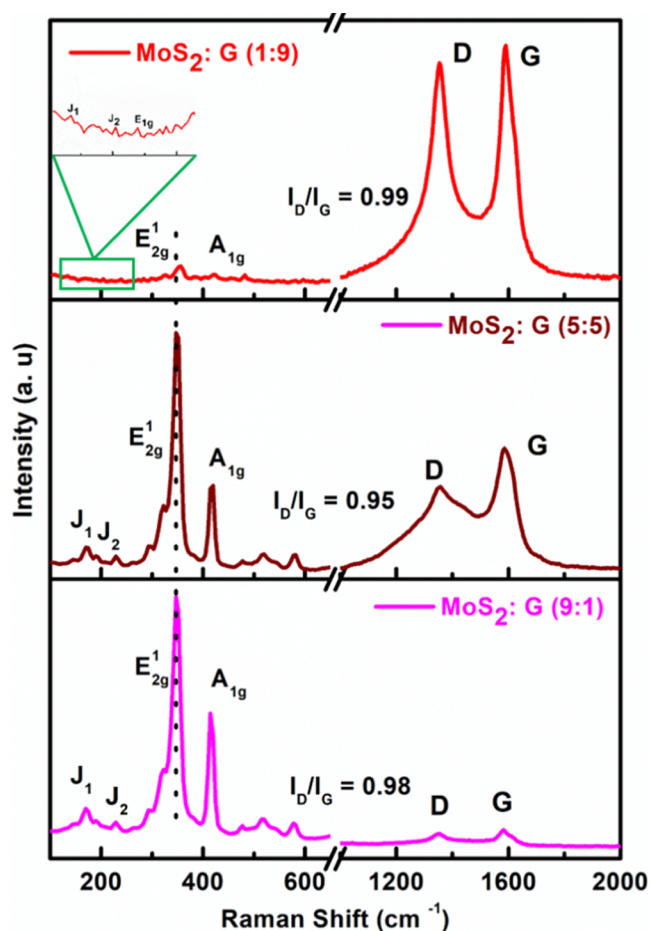
**Figure 2.** Raman spectra of MoS$_2$:G (9:1, 5:5, and 1:9) composites.

and S2) stimulated by a 532 nm laser. The composites show four Raman peaks in their spectra, and MoS$_2$ and graphene are responsible for their distinctive peaks. Two distinctive peaks at 350 and 415 cm$^{-1}$, which correspond to the E$_{2g}^1$ and A$_{1g}$ modes of hexagonal MoS$_2$, are seen at low wavenumbers. These Raman shifts are a result of the S–Mo–S layer first-order Raman vibration modes. The opposite vibration of the

Mo atoms with regard to two S atoms is responsible for the in-plane E$_{2g}^1$ mode, while the out-of-plane vibration of only S atoms in opposite directions is responsible for the A$_{1g}$ mode.[29] Apart from these two modes, three more peaks, J$_1$, J$_2$, and E$_{1g}$ (138, 204, and 245 cm$^{-1}$), are present in the spectrum, which clearly indicates the 1T-MoS$_2$ formed in 2H-MoS$_2$ in the composites.[30−33] After the MoS$_2$ was combined with graphene, the relative intensity of the J$_1$ peak was combined with A$_{1g}$, which can be used to estimate the 1T/2H conversion ratio. The composite materials show higher 1T/2H conversion ratios than pristine MoS$_2$, and especially the MoS$_2$/graphene (1:9) composite shows a higher intensity than the remaining two composites. This is expected as the possibility of MoS$_2$ layers stacking together to create the 2H phase is higher when there are fewer graphene layers present.[34,35]

In addition, it shows how well graphene and MoS$_2$ interact when they are stacked.[36] The characteristic D and G peaks from graphene also appear for the composites, suggesting homogeneous mixing. Apart from the above two modes, the Raman spectroscopy shows two more peaks, D and G, located at 1361 and 1601 cm$^{-1}$, respectively. The D band is attributed to the vibrations of carbon atoms with dangling bonds for the in-plane terminations of disordered graphite, while the G band is the result of the E$_{2g}$ mode (stretching vibrations) in the basal plane of crystalline graphite. From the results, the intensity ratio of the D and G bands ($I_D/I_G$) of the composites follows the order MoS$_2$/graphene (5:5) < MoS$_2$/graphene (9:1) < MoS$_2$/graphene (1:9) (0.95 < 0.98 < 0.99), which demonstrates that mass defects are introduced into the structure of the composite MoS$_2$/graphene (1:9).

The surface area and pore-size distribution of the as-prepared samples were calculated by using nitrogen (N$_2$) adsorption−desorption isotherm measurements. For pristine MoS$_2$ and graphene and the composites of Graphene:MoS$_2$ (1:9, 5:5, and 9:1), Figure 3 displays the corresponding N$_2$ adsorption−desorption isotherms and the Barrett−Joyner−Halenda (BJH) pore-size distribution map (1:9, 5:5, and 9:1). Figure 3a depicts N$_2$ adsorption/desorption isotherms of the samples; the type IV isotherms with hysteresis loops in the relative pressure ($P/P_0$) range of 0.4−1.0 demonstrate that the porosity of the nanocomposite is mostly made up of micro- and mesoporous materials. The specific surface areas of
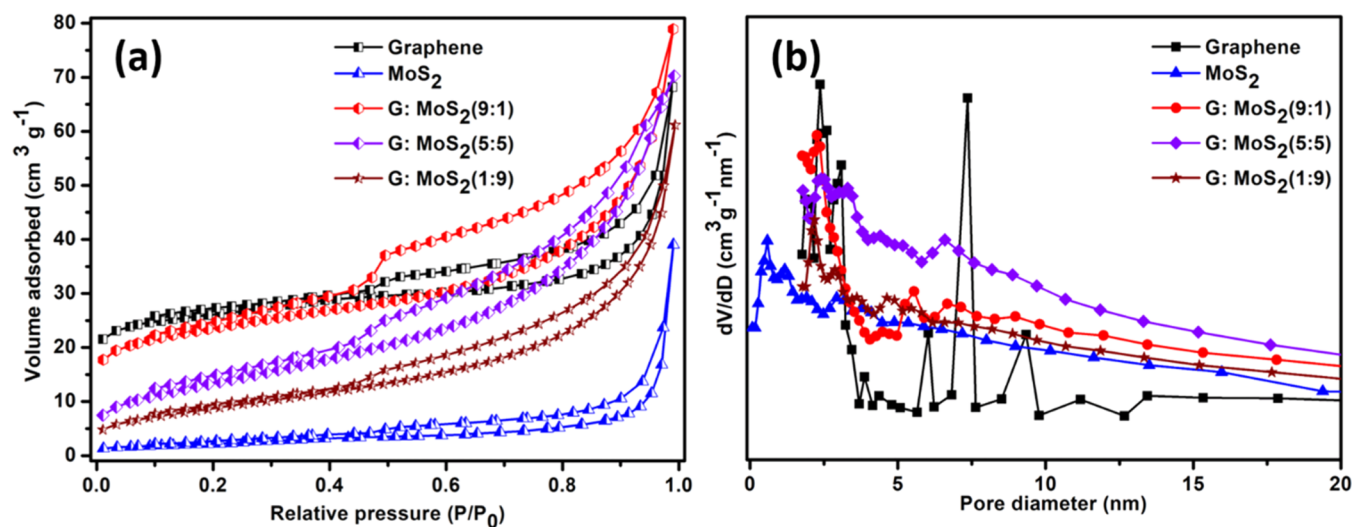


**Figure 3.** (a) N$_2$ sorption isotherms and (b) pore size distribution of pristine graphene, MoS$_2$, and G:MoS$_2$ (9:1, 5:5, and 1:9) composites.
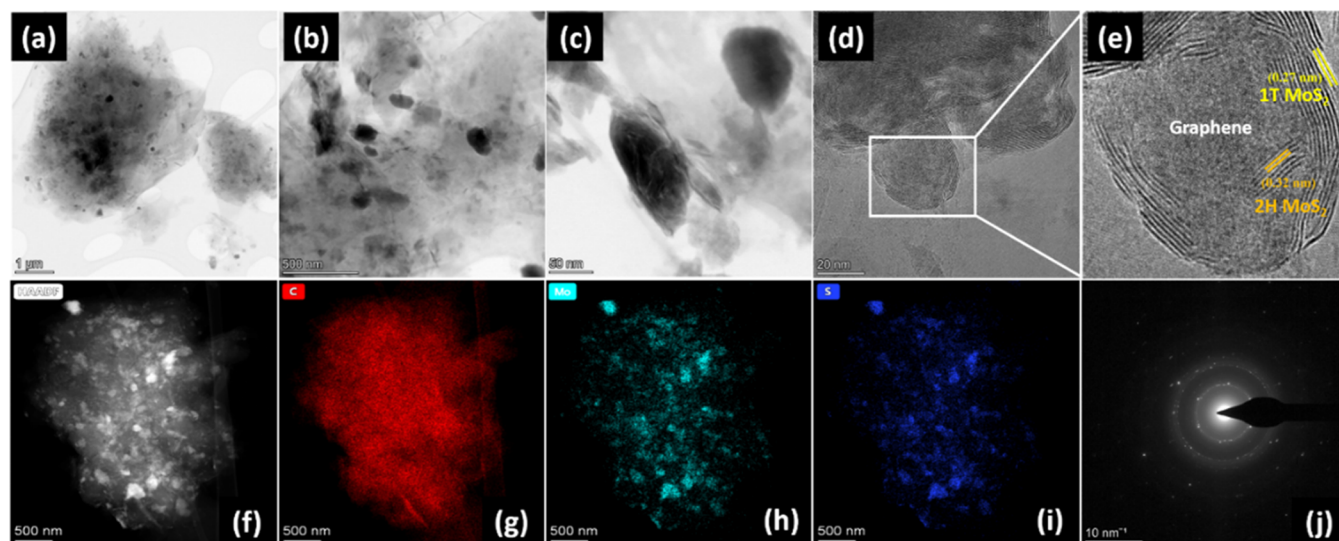
**Figure 4.** (a, b, and c) TEM images of the 9:1 ratio of the G:MoS$_2$ composite at different magnifications. (d) HRTEM image and (e) lattice fringes of the 9:1 ratio of the G:MoS$_2$ composite. (f) TEM image and elemental mapping of (g) C, (h) Mo, (i) S, and (j) SAED of the 9:1 ratio of the G:MoS$_2$ composite.

pristine graphene and MoS$_2$ and composites (G:MoS$_2$) with ratios of 9:1, 5:5, and 1:9 were 85, 8, 98, 49, and 32 m$^2$/g, respectively, indicating that G:MoS$_2$ (9:1) had a higher specific surface area compared to the remaining composites and pristine graphene and MoS$_2$ materials. However, the specific surface area of G:MoS$_2$ (9:1) is less than that of activated carbon materials, which affects the electrochemical properties. In addition, the Barrett−Joyner−Halenda pore size distribution curve of 9:1 (G:MoS$_2$), derived from the N$_2$ desorption plot, confirms the existence of >5 nm pores in the sample, as shown in the inset in Figure 3b. The space between graphene and MoS$_2$ makes it simple to understand this pore form. The high surface area and connected network of the conductive 9:1 (G:MoS$_2$) membrane are helpful for the creation of high-performance and flexible SCs.[37] The increased surface area of the 9:1 (G:MoS$_2$) nanocomposite is also anticipated to enable the establishment of an electrode/electrolyte interface that is most desired for ion accumulation.[38] Similar to this, it is considered that the presence of micro- and mesopores in the 9:1 (G:MoS$_2$) composite is advantageous for a high rate performance by permitting rapid ion accumulation, which may be the cause for the improved electrochemical performance.

High-resolution transmission electron microscopy (HRTEM) was used to better explore the internal architectures of pristine graphene and MoS$_2$ and the G:MoS$_2$ nanocomposites (9:1, 5:5, and 1:9) (Figures 4 and S3−S5). MoS$_2$ nanoparticles in the 50−60 nm size range are present, and they are distributed uniformly over the layers of graphene in the 9:1 G:MoS$_2$ composite (Figure 4a,c). The fact that the graphene sheets trap and arrange many MoS$_2$ nanoparticles like peas in a pod rather than producing conformal layers on individual particles is quite intriguing. This additional benefit of the morphological characteristics guarantees efficient electronic conductivity of each MoS$_2$ nanoparticle. In addition, by providing a spare space, the entire wrapping of nanocrystalline MoS$_2$ particles in graphene sheets significantly reduces the potentially enormous volume changes that the individual particles undergo during the charge/discharge process. However, the remaining two nanocomposites (G:MoS$_2$: 5:5 and 1:9) show agglomeration and volume change of MoS$_2$ due

to insufficient graphene (Figures S3 and S4) and affect the charge/discharge process. Figure 4d,e, displays the lattice fringes of the 9:1 (G:MoS$_2$) nanocomposite. The yellow and orange lines in Figure 4e show the lattice fringes with interplane spacings of 0.27 and 0.32 nm corresponding to the interlayer distance at the (100) plane of 1T-MoS$_2$ and 2H-MoS$_2$, respectively.[39−41] Figure 4f−i shows the elemental mapping corresponding to the HRTEM image of the 9:1 (G:MoS$_2$) nanocomposite, confirming the uniform dispersion of Mo and S elements throughout graphene (C). The selected-area electron diffraction (SAED) pattern of the 9:1 (G:MoS$_2$) nanocomposite, given in the inset of Figure 4j, indicates the polycrystalline nature of irregular nanoparticles. This suggests the successful combining of MoS$_2$ and graphene during the ball-milling and sonication process.

**4.1. Mechanism of Ionic Conductivity in the PVA-KOH Gel Electrolyte.** The PVA-KOH gel electrolyte was prepared by incorporating KOH and water molecules into the PVA matrix. The as-prepared PVA-KOH gel electrolyte was characterized by XRD, FTIR spectroscopy, and DSC. The X-ray diffraction pattern of pure PVA and PVA-KOH-based GPE films are shown in Figure S6. In the pattern of PVA, a peak at $2\theta = 19.6°$ is observed, showing the semicrystalline nature of PVA.[42] On adding KOH to PVA, this peak becomes very weak, and the combined system is almost amorphous in nature. Figure S7 compares the DSC curves of pure PVA with those of PVA-KOH gel electrolytes. The FTIR spectra (Figure S8) clearly depict the incorporation of the KOH solution inside the membranes, which is consistent with the results of the XRD.

The addition of KOH and water makes the PVA highly ionically conducting.[43] Notably, the ionic conductivity of the PVA-KOH gel is highly dependent on the amount of KOH and water molecules present within the gel (2.2:4.4 (KOH/H$_2$O), with 3.36 and 6.64 g, respectively).[42] For instance, the ionic conductivity of the PVA-KOH gel electrolyte was reported to be as high as $4.7 \times 10^{-2}$ S cm$^{-1}$ (PVA/KOH/H$_2$O = 30:30:40 wt %).[44] The ionic transport in the PVA-KOH gel membrane presumably occurs through the association and dissociation of ions between the polar groups of PVA chains (the Grotthuss mechanism). This phenomenon
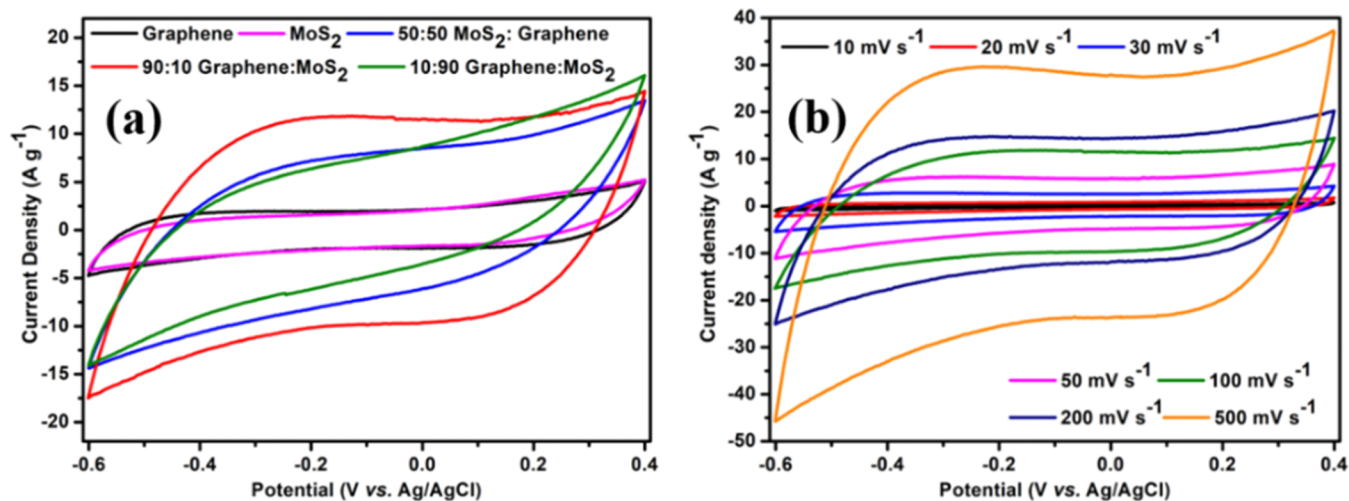
**Figure 5.** Electrochemical performance of electrodes (pristine graphene, MoS$_2$, and MoS$_2$:G (9:1, 5:5, and 1:9) composites) tested in a three-electrode configuration using 6 M KOH as the electrolyte. (a) CV curves of pristine graphene, MoS$_2$, and MoS$_2$:G (9:1, 1:1, and 1:9) composite electrodes at a scan rate of 100 mV s$^{-1}$. (b) CV curves of the MoS$_2$:G (1:9) composite electrode at different scan rates.

of association and dissociation of ions between the polymer chains is highly favorable when there is a higher concentration of KOH and water molecules in the gel. In addition, the increase in ionic mobility is related to the segmental motion of PVA chains, which creates a large free volume and ionic pathways.[19]

We examined and compared the electrochemical properties of pristine MoS$_2$, graphene, and MoS$_2$/graphene nanocomposites individually as the electrode material in both three- (Figure S9) and two-electrode configurations for SC applications in order to show the impact of graphene as a composite additive to MoS$_2$ in improving the capacitor performance. Figure 5a shows CV curves of pristine MoS$_2$, graphene, and MoS$_2$/graphene nanocomposites in the same potential window (−0.6 to 0.4 V) in a basic medium (6 M KOH) at a scan rate of 100 mV s$^{-1}$ using a three-electrode system. The rectangular curves of MoS$_2$/graphene nanocomposite electrodes are much higher than those of the pristine graphene and MoS$_2$ electrodes because the nanocomposite electrodes have a higher active specific surface area with the electrolyte than the pristine electrodes. Thus, the capacitances of the pristine graphene and MoS$_2$ electrodes are lower than those of the nanocomposite electrodes. The CV curves of G:MoS$_2$ (1:9 and 5:5) composites have a shuttle form due to the weak contact force between MoS$_2$ and graphene, but the G:MoS$_2$ (9:1) electrode exhibits capacitive behavior with an approximately rectangular form, thanks to the EDLC of the graphene material. The electronic transmission channel between MoS$_2$ and MoS$_2$ is shortened by the graphene layer, which also aids in the transfer of electrons or electrolyte ions.[37]

**4.2. Electrochemical Characterization.** For further analysis of the properties of the G:MoS$_2$ (9:1) composite electrode, Figure 5b shows the CV curves of the composite electrode at various scan rates. The CV curves of the MoS$_2$:G (1:9) composite electrode at various scan rates between 10 and 500 mV s$^{-1}$ have rectangular forms, which shows that the sample exhibits satisfactory capacitive behavior and good cycle reversibility.[45] The current response increases with an increase in the scan rate and can be explained by the fact that the diffusion layer becomes thinner and more electrolytic ions

interact with the electrode material. The CV curves of the G:MoS$_2$ (9:1) composite are symmetric without obvious deviation, which shows considerable reversibility and capacitive properties with a varying scan rate. However, no peak was observed at various scan rates, indicating that the electrode is charged and discharged at a constant EDLC rate during the whole voltammetric cycle. In addition, even at high scan rates, the CV curves maintain their shape, demonstrating an exceptionally high rate performance.

Figure 6a shows the CV curves of the as-prepared SC at various scan rates with the freestanding electrodes (Figure S10), exhibiting quasi-rectangular shapes. Figure 6b illustrates the galvanic charge/discharge (GCD) data that were used to further analyze the capacitive performance of the electrodes. The GCD curves demonstrate that they are roughly symmetrical at current densities of 5 A g$^{-1}$, demonstrating that the G:MoS$_2$ (9:1) composite exhibits higher capacitance than other composites, as well as pure graphene and MoS$_2$. The calculated specific capacitance of the G:MoS$_2$ (9:1) composite at a current density of 5 A g$^{-1}$ is 248 F g$^{-1}$, which is 6.2, 5.1, 1.3, and 1.2 times higher than those of graphene (40 F g$^{-1}$), MoS$_2$ (48 F g$^{-1}$), 1:1 (graphene:MoS$_2$) (180 F g$^{-1}$), and 1:9 (graphene:MoS$_2$) (210 F g$^{-1}$) electrodes, respectively. Notably, the specific capacitance of the G:MoS$_2$ (9:1) composite is also higher than those of most of the graphene-based and other SC materials[46−62] (Table 1).

The GCD profiles of graphene:MoS$_2$ (9:1) composite symmetric electrode are shown in Figure 6d for various current densities, from 1 to 20 A g$^{-1}$, in the potential range of 0−1.0 V. At various current densities, all curves were roughly linear and symmetrical, which supports the fact that the composite electrode made of graphene and MoS$_2$ (9:1) has strong reversibility. The triangular GCD curves show a significant double-layer capacitance contribution from carbon, and the graphene:MoS$_2$ (9:1) triangularity was out of shape, which was attributed to the pseudocapacitance of MoS$_2$. With an increase in the current density, the charge/discharge period was shortened. This can be explained by the fact that at high current densities, the contact between the electrode and electrolyte is restricted to the surface and does not have enough time to penetrate the electrode material. The
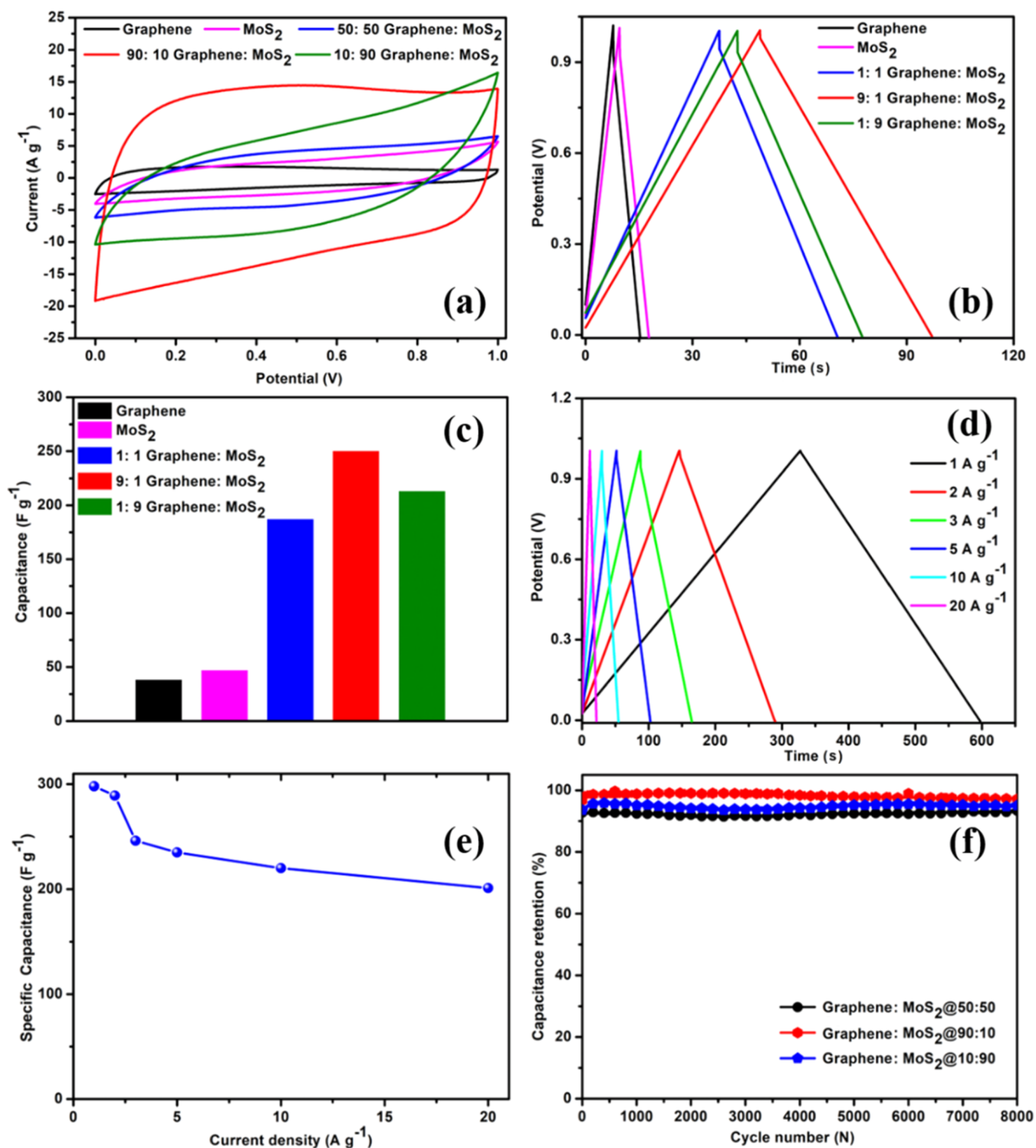
**Figure 6.** Electrochemical characterization of symmetric graphene, MoS$_2$, and graphene and MoS$_2$ composites with different ratios (1:1, 9:1, and 1:9) with the freestanding electrode device (coin cell). (a) CV curves of pristine graphene, MoS$_2$, and composites of graphene and MoS$_2$ (1:1, 9:1, and 1:9) with different ratios at a scan rate of 100 mV s$^{-1}$. (b) GCD curves of the graphene, MoS$_2$, and graphene and MoS$_2$ composites (1:1, 9:1, and 1:9) at a current density of 5 A g$^{-1}$. (c) Comparison of the capacitance. (d) GCD curves collected at different current densities (1, 2, 3, 5, 10, and 20 A g$^{-1}$). (e) Specific capacitance calculated from the charge/discharge curves as a function of current density. (f) Capacitance retention with respect to cycle number at a current density of 5 A g$^{-1}$.

characteristics of the GCD curves showed no appreciable departure over the wide range of current densities, demonstrating the stability of the graphene:MoS$_2$ (9:1) composite. At the lowest current density of 1 A g$^{-1}$, the specific capacitance of the graphene:MoS$_2$ (9:1) composite

was 295 F g$^{-1}$, and it retained 201 F g$^{-1}$ at the highest current density of 20 A g$^{-1}$ (Figure 6e).

Galvanostatic charge/discharge tests were conducted on the cycle life at a rate of 5 A g$^{-1}$ (Figures 6f and S11). After 8000 cycles, the composite samples show good charge/discharge

**Table 1. Comparison of the Current Work's Specific Capacitance with Previously Published Research**

| electrode materials | electrolyte | current density (A g$^{-1}$) | capacitance (F g$^{-1}$) | capacitance retention | ref |
|---|---|---|---|---|---|
| PANI-G-MoS$_2$ | 1 M H$_2$SO$_4$ | 0.9 | 142 | 98.11% | 46 |
| MoS$_2$/graphene (ball-milling) | 1 M H$_2$SO$_4$ | 1 | 280 | | 47 |
| MoS$_2$/rGO (ball-milling) | 1 M H$_2$SO$_4$ | 1 | 250 | | 48 |
| layered MoS$_2$/graphene | 1 M Na$_2$SO$_4$ | 1 | 250 | 92.3% up to 1000 cycles | 49 |
| 3D MoS$_2$/CMG | 1 M Na$_2$SO$_4$ | 1 | 257 | 93% up to 1000 cycles | 50 |
| MoS$_2$@G/AC | 3 M KOH | 1 | 255 | 83.8% up to 5000 cycles | 51 |
| MoS$_2$(L)-RGO composite | 1 M H$_2$SO$_4$ | 1 | 270 | 90% up to 5000 cycles | 52 |
| Pt-doped MoS$_2$ | 1 M of Na$_2$SO$_4$ | 0.5 | 250 | 87.96% up to 3000 cycles | 53 |
| MoS$_2$ nanosheets on titanium plates | 1 M KCl | 1 | 133 | 93% up to 1000 cycles | 54 |
| MoS$_2$ composite with activated carbon | 1 M Na$_2$SO$_4$ | | 179 | 89% up to 5000 cycles | 55 |
| MoS$_2$/CB-C | 1 M Na$_2$SO$_4$ | 1 | 333.5 | 81.8% up to 7000 cycles | 56 |
| MoS$_2$/CNT | 1 M Na$_2$SO$_4$ | 1 | 75 | 80% up to 1000 cycles | 57 |
| 2D-MoS$_2$ | 3 M KOH | 0.5 | 186 | | 58 |
| MoS$_2$/SnO$_2$ | 2 M KOH | 1 | 66 | 90% up to 1000 cycles | 59 |
| MoS$_2$@3D porous graphene | 1 M LiPF$_6$/EC/DMC/EMC | 0.1 | 88.3 | 78% up to 2000 cycles | 60 |
| MoS$_2$/reduced graphene oxide | 2 M KOH | 1 | 218 | 92% up to 1000 cycles | 61 |
| h-rGO@MoS$_2$ | 1 M Na$_2$SO$_4$ | 0.5 | 238 | 88% up to 3500 cycles | 62 |
| this work | 6 M KOH | 1 | 295 | 99.0% up to 8000 cycles | this work |

stability compared with pristine graphene and MoS$_2$ (Figure S11). The capacity retention for graphene, MoS$_2$, and nanocomposites of 5:5, 1:9, and 9:1 were 89, 86, 92, 94.5, and 97.3%, respectively. The volume instability of MoS$_2$ under the external current leads to the detachment of MoS$_2$ from the scaffold network, which contributes to the poor cycling stability of the 5:5 (G:MoS$_2$) and 1:9 (G:MoS$_2$) composites. The superior capacitive behavior of 9:1 (G:MoS$_2$) is a result of the synergy between the electric double-layer capacitance (EDLC) and the pseudocapacitance because of redox processes in the presence of MoS$_2$, with increased specific surface area and uniform dispersion of MoS$_2$ on graphene. These findings unambiguously show that 9:1 (G:MoS$_2$) is a more effective supercapacitor electrode material than the remaining composite (5:5 and 1:9 (G:MoS$_2$)), pristine graphene, and MoS$_2$ electrode materials. For this reason, flexible solid-state supercapacitors used the 9:1 (G:MoS$_2$) composite as the electrode material.

Figure S12 displays the Nyquist plot for the electrochemical performances of graphene, MoS$_2$, and graphene:MoS$_2$ (1:9, 1:1, and 9:1) composite electrodes, which were further studied by EIS in the frequency range of 100 Hz to 10 kHz (Supporting Information). Except for the pristine MoS$_2$ and composite MoS$_2$:G (9:1) electrodes, all charts have almost vertical lines in the low-frequency range, which denotes a nearly optimal capacitive behavior. The intercept of a quasi-semicircle in the x-axis can be used to depict the equivalent series resistance (ESR), which includes the intrinsic resistance of the materials and the ionic resistance of the electrolyte at high frequencies ($R_s$). In addition, the diameter of the semicircle is used to determine the charge transfer resistance, which is a result of the Faradaic reaction and double-layer capacitance at the electrode/electrolyte interface. By extrapolating, the $R_{ct}$ and $R_s$ values of the graphene, MoS$_2$, and graphene:MoS$_2$ (1:9, 5:5, and 9:1) composite electrodes were found to be 6.3, 65, 20, 3.4, and 5.1 W and 0.5, 1.4, 0.8, 0.7, and 0.3, respectively. Both $R_{ct}$ and $R_s$ were high when MoS$_2$ was loaded heavily, indicating that the diffusion of electrolyte ions and their interactions with electrode materials gradually deteriorated. From this observation, a high mass loading of

MoS$_2$ obstructs effective electrolyte ion diffusion within the electrode due to the aggregation of metal sulfides. The low ESR values ($R_{ct}$ and $R_s$) of the graphene:MoS$_2$ (9:1) composite electrode due to graphene increased the conductivity and facilitated the transport of the electrons and electrolyte ions from the electrode to the electrolyte interface. Moreover, the graphene:MoS$_2$ (9:1) composite electrode exhibited a larger slope in the low-frequency region than the remaining electrodes, demonstrating a higher internal ion diffusion rate.[63-67] All of these findings indicate that the high-surface-area graphene:MoS$_2$ (9:1) composite electrode has a lower charge transfer impedance at the electrode–electrolyte interface and a higher internal electron transport velocity than the graphene, MoS$_2$, and graphene:MoS$_2$ composite electrodes (1:1 and 1:9). As a result, the composite electrode made of graphene and MoS$_2$ (9:1) has a higher $C_{sp}$ than the other electrodes.

Two important parameters that determine how well SCs may be used as power sources are their energy and power densities. The Ragone plots of graphene and MoS$_2$ (9:1) nanocomposites are shown in Figure 7. Equations 2 and 3 are used to calculate the specific energy density ($E$) and specific power density ($P$) of the graphene and MoS$_2$ (9:1) electrodes. According to the Ragone plot, the energy density steadily decreases as the power density increases. Graphene and MoS$_2$ (9:1) have energy densities that were on par with or higher than those reported in the most recent studies.[49,56,63,68-71] The high surface area and uniform distribution of MoS$_2$ in graphene, which is obtained from the straightforward ball-milling approach, are responsible for the superior electrochemical performance of the device.

A solid-state flexible device offers several desirable advantages over typical liquid-based SCs, including ease of handling, scalability, flexibility, better safety, and a broad operating temperature range. Two electrodes of graphene:-MoS$_2$ (9:1) (Figure S10, digital image of the electrode) films were used in the current work to create a flexible symmetric SC device, with the PVA-KOH gel serving as the electrolyte (as seen in Figure 8b, inset). As shown in Figure 8, the electrochemical performance was examined at room temper-
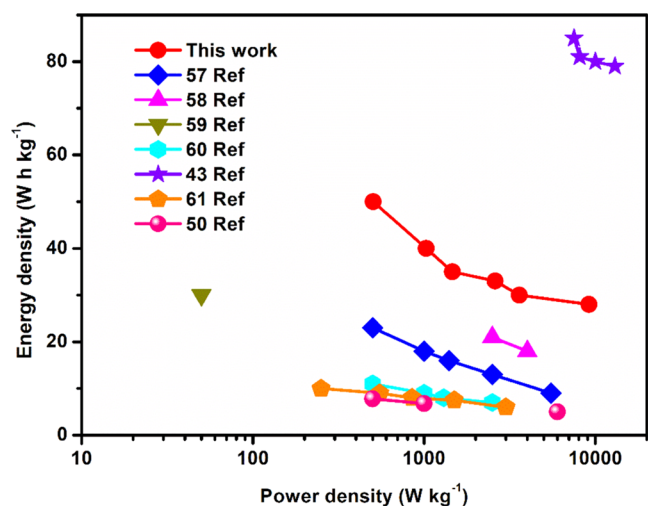
**Figure 7.** Comparison of the energy and power density reported for the G:MoS$_2$ (9:1) supercapacitor in the recent literature on MoS$_2$ supercapacitors.

ature. The CV curves of the as-prepared SC are displayed in Figure 8a with quasi-rectangular forms at different scan rates

and voltage windows from 0.0 to 1.0 V. The quasi-rectangular shape indicates, at different scan rates, that the electrolyte ion suffers from a low diffusion rate in the gel electrolyte. Finally, the CV test of a flexible supercapacitor under various bending angles was performed at a 100 mV s$^{-1}$ scanning rate, as shown in Figure 8b, to investigate the flexibility of graphene:MoS$_2$ (9:1). The CV curves clearly show no changes when bent at different angles. In addition, we also studied the stability of a flexible supercapacitor under a bending angle of 180° for CV 8000 cycles. The CV curves almost overlap with each other even after 8000 cycles, indicating the excellent mechanical properties of the flexible supercapacitor. Further, the device was studied for long cycles at a current density of 1 A g$^{-1}$ for 8000 cycles in the bent state of 180° (Figure 8c). The device retains approximately 93% of its capacitance and Columbic efficiency after 8000 cycles (Figure 8d). It should be highlighted that the flexible supercapacitor received mechanical support from the graphene backbone, in addition to the extremely conductive channels.

## 5. CONCLUSIONS

This article describes the design and fabrication of an MoS$_2$/graphene composite electrode that is used directly as an
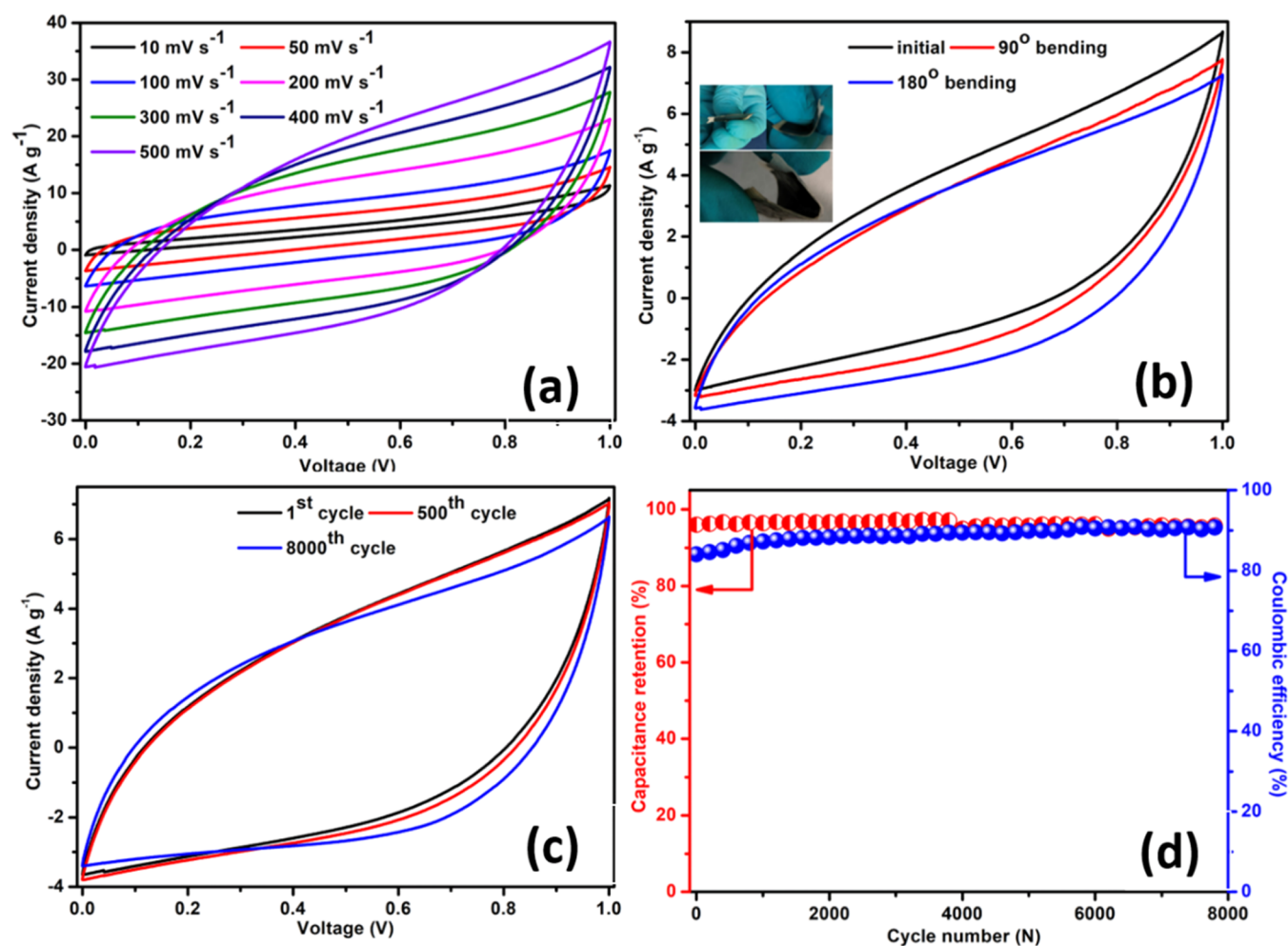


**Figure 8.** Electrochemical performance of the flexible supercapacitor device: (a) CV curves at different scan rates; (b) CV curves of the flexible supercapacitor device at 100 mV s$^{-1}$ under different bending angles (inset: digital images of the flat and bent (90 and 180°) states); (c) 1st, 500th, and 8000th CV curves of the flexible supercapacitor; and (d) capacitance retention and Coulombic efficiency of the flexible supercapacitor device bending at 180°. (Image courtesy of Bongu Chandra Sekhar. Copyright 2023).

electrode for a SC. BET and HRTEM confirm the surface area and morphology of these materials. Further, an electrochemical study is carried out by a symmetric device where the composite ($MoS_2$/graphene, 1:9) is used as a freestanding electrode and 6 M KOH as the electrolyte. At a discharge density of 5 A $g^{-1}$, the as-developed $MoS_2$/graphene (1:9) electrode exhibits an outstanding specific capacitance of 248 F $g^{-1}$ and a capacitance retention of 97.3% after 8000 cycles. Furthermore, the all-solid-state flexible supercapacitor fabricated with the $MoS_2$/graphene (1:9) composite electrode shows excellent cycle performance (retains 93.0% after 8000 cycles). This improved electrochemical performance is due to the synergistic effects between $MoS_2$ and graphene sheets. The significant prospective uses of the $MoS_2$/graphene (1:9) composite electrode in energy storage for compact, lightweight, and flexible electronic devices is indicated by its superior electrochemical performance.

## ASSOCIATED CONTENT

### Ⓢ Supporting Information

The Supporting Information is available free of charge at https://pubs.acs.org/doi/10.1021/acsomega.3c03370.

> Raman spectra of the pristine graphene nanoplates (Figure S1) and pristine $MoS_2$ (Figure S2); TEM images of pristine graphene and $MoS_2$ (Figure S3); TEM, HRTEM, and corresponding magnified HRTEM images; TEM image and corresponding elemental mapping images of C, Mo, and S, and SAED of the 5:5 ratio of the G:$MoS_2$ composite (Figure S4) and the 1:9 ratio of the G:$MoS_2$ composite (Figure S5); XRD of the PVA film and PVA-KOH membrane (Figure S6); DSC curves of the PVA-KOH gel membrane and PVA film (Figure S7); FTIR spectra of the PVA film and PVA-KOH gel membrane (Figure S8); CV performances of pristine graphene, $MoS_2$, G:$MoS_2$ (5:5), G:$MoS_2$ (9:1), and G:$MoS_2$ (1:9) composite electrodes at different scan rates in a three-electrode system (Figure S9); digital image of the G:$MoS_2$ (9:1) composite electrode (Figure S10); capacitance retention of $MoS_2$ and graphene with respect to the cycle number at a current density of 5 A $g^{-1}$ (Figure S11); Nyquist plots of different samples over the frequency range of 100 kHz to 0.01 Hz (the inset shows a close-up view at a high frequency) (Figure S12) (PDF)

## AUTHOR INFORMATION

### Corresponding Author

**Edreese H. Alsharaeh** — *College of Science and General Studies, Alfaisal University, Riyadh 11533, Saudi Arabia;* ⊙ orcid.org/0000-0002-3707-7883; Email: ealsharaeh@ alfaisal.edu

### Authors

**Chandra Sekhar Bongu** — *College of Science and General Studies, Alfaisal University, Riyadh 11533, Saudi Arabia*

**Mohan Raj Krishnan** — *College of Science and General Studies, Alfaisal University, Riyadh 11533, Saudi Arabia*

**Abdelrahman Soliman** — *College of Science and General Studies, Alfaisal University, Riyadh 11533, Saudi Arabia*

**Muhammad Arsalan** — *EXPEC Advanced Research Center, Saudi Aramco, Dhahran 31311, Saudi Arabia;* ⊙ orcid.org/ 0000-0002-1502-8247

Complete contact information is available at:
https://pubs.acs.org/10.1021/acsomega.3c03370

### Notes

The authors declare no competing financial interest.

## ■ REFERENCES

(1) Wang, G.; Zhang, L.; Zhang, J. A Review of Electrode Materials for Electrochemical Supercapacitors. *Chem. Soc. Rev.* **2012**, *41* (2), 797−828.

(2) Inagaki, M.; Konno, H.; Tanaike, O. Carbon Materials for Electrochemical Capacitors. *J. Power Sources* **2010**, *195* (24), 7880−7903.

(3) Hou, Y.; Cheng, Y.; Hobson, T.; Liu, J. Design and Synthesis of Hierarchical MnO2 Nanospheres/Carbon Nanotubes/Conducting Polymer Ternary Composite for High Performance Electrochemical Electrodes. *Nano Lett.* **2010**, *10* (7), 2727−2733.

(4) Cheng, Y.; Lu, S.; Zhang, H.; Varanasi, C. V.; Liu, J. Synergistic Effects from Graphene and Carbon Nanotubes Enable Flexible and Robust Electrodes for High-Performance Supercapacitors. *Nano Lett.* **2012**, *12* (8), 4206−4211.

(5) Huang, G.; Chen, T.; Chen, W.; Wang, Z.; Chang, K.; Ma, L.; Huang, F.; Chen, D.; Lee, J. Y. Graphene-Like MoS2/Graphene Composites: Cationic Surfactant-Assisted Hydrothermal Synthesis and Electrochemical Reversible Storage of Lithium. *Small* **2013**, *9* (21), 3693−3703.

(6) Mayorga-Martinez, C. C.; Moo, J. G. S.; Khezri, B.; Song, P.; Fisher, A. C.; Sofer, Z.; Pumera, M. Self-propelled Supercapacitors for On-demand Circuit Configuration Based on WS2 Nanoparticles Micromachines. *Adv. Funct. Mater.* **2016**, *26* (36), 6662−6667.

(7) Feng, J.; Sun, X.; Wu, C.; Peng, L.; Lin, C.; Hu, S.; Yang, J.; Xie, Y. Metallic Few-Layered VS2 Ultrathin Nanosheets: High Two-Dimensional Conductivity for in-Plane Supercapacitors. *J. Am. Chem. Soc.* **2011**, *133* (44), 17832−17838.

(8) Acerce, M.; Voiry, D.; Chhowalla, M. Metallic 1T Phase MoS2 Nanosheets as Supercapacitor Electrode Materials. *Nat. Nanotechnol.* **2015**, *10* (4), 313−318.

(9) Yang, Y.; Fei, H.; Ruan, G.; Xiang, C.; Tour, J. M. Edge-oriented MoS2 Nanoporous Films as Flexible Electrodes for Hydrogen Evolution Reactions and Supercapacitor Devices. *Adv. Mater.* **2014**, *26* (48), 8163−8168.

(10) Rao, C. N. R.; Sood, A. K.; Subrahmanyam, K. S.; Govindaraj, A. Graphene: The New Two-dimensional Nanomaterial. *Angew. Chem., Int. Ed.* **2009**, *48* (42), 7752−7777.

(11) Yang, M.; Ko, S.; Im, J. S.; Choi, B. G. Free-Standing Molybdenum Disulfide/Graphene Composite Paper as a Binder-and Carbon-Free Anode for Lithium-Ion Batteries. *J. Power Sources* **2015**, *288*, 76−81.

(12) Wang, J.-Z.; Lu, L.; Lotya, M.; Coleman, J. N.; Chou, S.; Liu, H.; Minett, A. I.; Chen, J. Development of MoS2−CNT Composite Thin Film from Layered MoS2 for Lithium Batteries. *Adv. Energy Mater.* **2013**, *3* (6), 798−805.

(13) Sha, C.; Lu, B.; Mao, H.; Cheng, J.; Pan, X.; Lu, J.; Ye, Z. 3D Ternary Nanocomposites of Molybdenum Disulfide/Polyaniline/ Reduced Graphene Oxide Aerogel for High Performance Supercapacitors. *Carbon* **2016**, *99*, 26−34.

(14) Zhou, F.; Xin, S.; Liang, H.; Song, L.; Yu, S. Carbon Nanofibers Decorated with Molybdenum Disulfide Nanosheets: Synergistic Lithium Storage and Enhanced Electrochemical Performance. *Angew. Chem., Int. Ed.* **2014**, *53* (43), 11552−11556.

(15) Bai, Z.; Zhang, Y.; Zhang, Y.; Guo, C.; Tang, B. Hierarchical MoS2@ Carbon Microspheres as Advanced Anodes for Li-ion Batteries. *Chem. — Eur. J.* **2015**, *21* (50), 18187−18191.

(16) Jiang, S.; Zhou, X.; Xiao, H.; Chen, W.; Xu, X.; Liu, Z. Robust and Durable Flexible Micro-Supercapacitors Enabled by Graphene Nanoscrolls. *Chem. Eng. J.* **2021**, *405*, No. 127009.

(17) Chang, Q.; Li, L.; Sai, L.; Shi, W.; Huang, L. Water-Soluble Hybrid Graphene Ink for Gravure-Printed Planar Supercapacitors. *Adv. Electron. Mater.* **2018**, *4* (8), No. 1800059.

(18) Beidaghi, M.; Wang, C. Micro-supercapacitors Based on Interdigital Electrodes of Reduced Graphene Oxide and Carbon Nanotube Composites with Ultrahigh Power Handling Performance. *Adv. Funct. Mater.* **2012**, *22* (21), 4501−4510.

(19) Velez, A. A. I.; Reyes, E.; Diaz-Barrios, A.; Santos, F.; Fernández Romero, A. J.; Tafur, J. P. Properties of the PVA-VAVTD KOH Blend as a Gel Polymer Electrolyte for Zinc Batteries. *Gels* **2021**, *7* (4), 256.

(20) Aslam, M.; Kalyar, M. A.; Raza, Z. A. Polyvinyl Alcohol: A Review of Research Status and Use of Polyvinyl Alcohol Based Nanocomposites. *Polym. Eng. Sci.* **2018**, *58* (12), 2119−2132.

(21) Goodship, V.; Jacobs, D. *Polyvinyl Alcohol: Materials, Processing and Applications* Smithers Rapra Technology: Shrewsbury, Shropshire; 2009.

(22) Xu, C.; Zhang, D. Multifunctional Structural Supercapacitor Based on Cement/PVA-KOH Composite and Graphene. *J. Compos. Mater.* **2021**, *55* (10), 1359−1369.

(23) Pandit, B.; Sankapal, B. R. Cerium Selenide Nanopebble/ Multiwalled Carbon Nanotube Composite Electrodes for Solid-State Symmetric Supercapacitors. *ACS Appl. Nano Mater.* **2022**, *5* (2), 3007−3017.

(24) Goda, E. S.; ur Rehman, A.; Pandit, B.; Eissa, A. A.-S.; Hong, S. E.; Yoon, K. R. Al-Doped Co9S8 Encapsulated by Nitrogen-Doped Graphene for Solid-State Asymmetric Supercapacitors. *Chem. Eng. J.* **2022**, *428*, No. 132470.

(25) Pandit, B.; Agarwal, A.; Patel, P.; Sankapal, B. R. The Electrochemical Kinetics of Cerium Selenide Nano-Pebbles: The Design of a Device-Grade Symmetric Configured Wide-Potential Flexible Solid-State Supercapacitor. *Nanoscale Adv.* **2021**, *3* (4), 1057−1066.

(26) Pandit, B.; Rondiya, S. R.; Cross, R. W.; Dzade, N. Y.; Sankapal, B. R. Vanadium Telluride Nanoparticles on MWCNTs Prepared by Successive Ionic Layer Adsorption and Reaction for Solid-State Supercapacitor. *Chem. Eng. J.* **2022**, *429*, No. 132505.

(27) Pandit, B.; Goda, E. S.; Abu Elella, M. H.; Elella, M. H. A.; ur Rehman, A.; Eun Hong, S.; Hong, S. E.; Rondiya, S. R.; Barkataki, P.; Shaikh, S. F.; Al-Enizi, A. M.; El-Bahy, S. M. One-Pot Hydrothermal Preparation of Hierarchical Manganese Oxide Nanorods for High-Performance Symmetric Supercapacitors. *J. Energy Chem.* **2022**, *65*, 116−126.

(28) Singh, K.; Kumar, S.; Agarwal, K.; Soni, K.; Ramana Gedela, V.; Ghosh, K. Three-Dimensional Graphene with MoS 2 Nanohybrid as Potential Energy Storage/Transfer Device. *Sci. Rep.* **2017**, *7* (1), No. 9458.

(29) Bertrand, P. A. Surface-Phonon Dispersion of MoS 2. *Phys. Rev. B* **1991**, *44* (11), 5745.

(30) Guo, C.; Pan, J.; Li, H.; Lin, T.; Liu, P.; Song, C.; Wang, D.; Mu, G.; Lai, X.; Zhang, H.; et al. Observation of Superconductivity in 1T′-MoS 2 Nanosheets. *J. Mater. Chem. C* **2017**, *5* (41), 10855−10860.

(31) Rao, C.; Maitra, U.; Waghmare, U. V. Extraordinary Attributes of 2-Dimensional MoS2 Nanosheets. *Chem. Phys. Lett.* **2014**, *609*, 172−183.

(32) Lukowski, M. A.; Daniel, A. S.; Meng, F.; Forticaux, A.; Li, L.; Jin, S. Enhanced Hydrogen Evolution Catalysis from Chemically Exfoliated Metallic MoS2 Nanosheets. *J. Am. Chem. Soc.* **2013**, *135* (28), 10274−10277.

(33) Zhang, P.; Gao, C.; Xu, B.; Qi, L.; Jiang, C.; Gao, M.; Xue, D. Structural Phase Transition Effect on Resistive Switching Behavior of

MoS2-polyvinylpyrrolidone Nanocomposites Films for Flexible Memory Devices. *Small* **2016**, *12* (15), 2077−2084.

(34) Zhuo, Y.; Prestat, E.; Kinloch, I. A.; Bissett, M. A. Self-Assembled 1T-MoS2/Functionalized Graphene Composite Electrodes for Supercapacitor Devices. *ACS Appl. Energy Mater.* **2022**, *5* (1), 61−70.

(35) Jeffery, A. A.; Rao, S. R.; Rajamathi, M. Preparation of MoS2− Reduced Graphene Oxide (RGO) Hybrid Paper for Catalytic Applications by Simple Exfoliation−Costacking. *Carbon* **2017**, *112*, 8−16.

(36) Zhou, K.-G.; Withers, F.; Cao, Y.; Hu, S.; Yu, G.; Casiraghi, C. Raman Modes of MoS2 Used as Fingerprint of van Der Waals Interactions in 2-D Crystal-Based Heterostructures. *ACS Nano* **2014**, *8* (10), 9914−9924.

(37) Wang, S.; Zhu, J.; Shao, Y.; Li, W.; Wu, Y.; Zhang, L.; Hao, X. Three-dimensional MoS2@ CNT/RGO Network Composites for High-performance Flexible Supercapacitors. *Chem. — Eur. J.* **2017**, *23* (14), 3438−3446.

(38) Xiao, X.; Peng, X.; Jin, H.; Li, T.; Zhang, C.; Gao, B.; Hu, B.; Huo, K.; Zhou, J. Freestanding Mesoporous VN/CNT Hybrid Electrodes for Flexible All-solid-state Supercapacitors. *Adv. Mater.* **2013**, *25* (36), 5091−5097.

(39) Shi, S.; Sun, Z.; Hu, Y. H. Synthesis, Stabilization and Applications of 2-Dimensional 1T Metallic MoS 2. *J. Mater. Chem. A* **2018**, *6* (47), 23932−23977.

(40) Fan, H.; Wu, R.; Liu, H.; Yang, X.; Sun, Y.; Chen, C. Synthesis of Metal-Phase-Assisted 1T@ 2H-MoS2 Nanosheet-Coated Black TiO2 Spheres with Visible Light Photocatalytic Activities. *J. Mater. Sci.* **2018**, *53* (14), 10302−10312.

(41) Cai, L.; Cheng, W.; Yao, T.; Huang, Y.; Tang, F.; Liu, Q.; Liu, W.; Sun, Z.; Hu, F.; Jiang, Y.; et al. High-Content Metallic 1T Phase in MoS2-Based Electrocatalyst for Efficient Hydrogen Evolution. *J. Phys. Chem. C* **2017**, *121* (28), 15071−15077.

(42) Santos, F.; Tafur, J. P.; Abad, J.; Fernández Romero, A. J. Structural Modifications and Ionic Transport of PVA-KOH Hydrogels Applied in Zn/Air Batteries. *J. Electroanal. Chem.* **2019**, *850*, No. 113380.

(43) Choudhury, N. A.; Sampath, S.; Shukla, A. Hydrogel-Polymer Electrolytes for Electrochemical Capacitors: An Overview. *Energy Environ. Sci.* **2009**, *2* (1), 55−67.

(44) Yang, C.-C.; Lin, S.-J. Preparation of Composite Alkaline Polymer Electrolyte. *Mater. Lett.* **2002**, *57* (4), 873−881.

(45) Zhao, C.; Zhou, Y.; Ge, Z.; Zhao, C.; Qian, X. Facile Construction of MoS2/RCF Electrode for High-Performance Supercapacitor. *Carbon* **2018**, *127*, 699−706.

(46) Palsaniya, S.; Nemade, H. B.; Dasmahapatra, A. K. Synthesis of Polyaniline/Graphene/MoS2 Nanocomposite for High Performance Supercapacitor Electrode. *Polymer* **2018**, *150*, 150−158.

(47) Ji, H.-M.; Luan, A.-L.; Dai, C.-C.; Li, M.; Yang, G.; Hou, W.-H. Highly Active Free-Standing and Flexible MoS2/RGO Sandwich-Structured Films for Supercapacitor Applications. *Solid State Commun.* **2019**, *297*, 45−49.

(48) Ji, H.; Hu, S.; Jiang, Z.; Shi, S.; Hou, W.; Yang, G. Directly Scalable Preparation of Sandwiched MoS2/Graphene Nanocomposites via Ball-Milling with Excellent Electrochemical Energy Storage Performance. *Electrochim. Acta* **2019**, *299*, 143−151.

(49) Huang, K.-J.; Wang, L.; Liu, Y.-J.; Liu, Y.-M.; Wang, H.-B.; Gan, T.; Wang, L.-L. Layered MoS2−Graphene Composites for Supercapacitor Applications with Enhanced Capacitive Performance. *Int. J. Hydrogen Energy* **2013**, *38* (32), 14027−14034.

(50) Yang, M.; Jeong, J.-M.; Huh, Y. S.; Choi, B. G. High-Performance Supercapacitor Based on Three-Dimensional MoS2/ Graphene Aerogel Composites. *Compos. Sci. Technol.* **2015**, *121*, 123−128.

(51) Fu, H.; Zhang, X.; Fu, J.; Shen, G.; Ding, Y.; Chen, Z.; Du, H. Single Layers of MoS2/Graphene Nanosheets Embedded in Activated Carbon Nanofibers for High-Performance Supercapacitor. *J. Alloys Compd.* **2020**, *829*, No. 154557.

(52) Hota, P.; Miah, M.; Bose, S.; Dinda, D.; Ghorai, U. K.; Su, Y.-K.; Saha, S. K. Ultra-Small Amorphous MoS2 Decorated Reduced Graphene Oxide for Supercapacitor Application. *J. Mater. Sci. Technol.* **2020**, *40*, 196−203.

(53) Shao, J.; Li, Y.; Zhong, M.; Wang, Q.; Luo, X.; Li, K.; Zhao, W. Enhanced-Performance Flexible Supercapacitor Based on Pt-Doped MoS2. *Mater. Lett.* **2019**, *252*, 173−177.

(54) Wang, L.; Ma, Y.; Yang, M.; Qi, Y. Titanium Plate Supported MoS2 Nanosheet Arrays for Supercapacitor Application. *Appl. Surf. Sci.* **2017**, *396*, 1466−1471.

(55) Sangeetha, D. N.; Selvakumar, M. Active-Defective Activated Carbon/MoS2 Composites for Supercapacitor and Hydrogen Evolution Reactions. *Appl. Surf. Sci.* **2018**, *453*, 132−140.

(56) Wang, F.; Ma, J.; Zhou, K.; Li, X. MoS2/Corncob-Derived Activated Carbon for Supercapacitor Application. *Mater. Chem. Phys.* **2020**, *244*, No. 122215.

(57) Chen, M.; Dai, Y.; Wang, J.; Wang, Q.; Wang, Y.; Cheng, X.; Yan, X. Smart Combination of Three-Dimensional-Flower-like MoS2 Nanospheres/Interconnected Carbon Nanotubes for Application in Supercapacitor with Enhanced Electrochemical Performance. *J. Alloys Compd.* **2017**, *696*, 900−906.

(58) Gupta, H.; Chakrabarti, S.; Mothkuri, S.; Padya, B.; Rao, T. N.; Jain, P. K. High Performance Supercapacitor Based on 2D-MoS2 Nanostructures. *Mater. Today: Proc.* **2020**, *26*, 20−24.

(59) Prabukumar, C.; Sadiq, M. M. J.; Bhat, D. K.; Bhat, K. U. SnO2 Nanoparticles Functionalized MoS2 Nanosheets as the Electrode Material for Supercapacitor Applications. *Mater. Res. Express* **2019**, *6* (8), No. 085526.

(60) Zhang, F.; Tang, Y.; Liu, H.; Ji, H.; Jiang, C.; Zhang, J.; Zhang, X.; Lee, C.-S. Uniform Incorporation of Flocculent Molybdenum Disulfide Nanostructure into Three-Dimensional Porous Graphene as an Anode for High-Performance Lithium Ion Batteries and Hybrid Supercapacitors. *ACS Appl. Mater. Interfaces* **2016**, *8* (7), 4691−4699.

(61) Xiao, W.; Zhou, W.; Feng, T.; Zhang, Y.; Liu, H.; Tian, L. Simple Synthesis of Molybdenum Disulfide/Reduced Graphene Oxide Composite Hollow Microspheres as Supercapacitor Electrode Material. *Materials* **2016**, *9* (9), 783.

(62) Zheng, S.; Zheng, L.; Zhu, Z.; Chen, J.; Kang, J.; Huang, Z.; Yang, D. MoS2 Nanosheet Arrays Rooted on Hollow RGO Spheres as Bifunctional Hydrogen Evolution Catalyst and Supercapacitor Electrode. *Nano−Micro Lett.* **2018**, *10* (4), 62.

(63) Bao, J.; Zeng, X.-F.; Huang, X.-J.; Chen, R.-K.; Wang, J.-X.; Zhang, L.-L.; Chen, J.-F. Three-Dimensional MoS2/RGO Nano-composites with Homogeneous Network Structure for Supercapacitor Electrodes. *J. Mater. Sci.* **2019**, *54* (24), 14845−14858.

(64) Goda, E. S.; Pandit, B.; Hong, S. E.; Singu, B. S.; Kim, S. K.; Moustafa, E. B.; Yoon, K. R. Zeolitic Imidazolate Framework-67 Derived Al-Co-S Hierarchical Sheets Bridged by Nitrogen-Doped Graphene: Incorporation of PANI Derived Carbon Nanorods for Solid-State Asymmetric Supercapacitors. *J. Energy Chem.* **2022**, *74*, 429−445.

(65) Pandit, B.; Sankapal, B. R. Chemically Processed Metal Oxides for Sensing Application: Heterojunction Room Temperature LPG Sensor. In *Chemically Deposited Nanocrystalline Metal Oxide Thin Films: Synthesis, Characterizations, and Applications*; Springer, 2021; pp 765−805.

(66) Khedulkar, A. P.; Dien Dang, V.; Pandit, B.; Bui, T. A. N.; Tran, H. L.; Doong, R. Flower-like Nickel Hydroxide@ Tea Leaf-Derived Biochar Composite for High-Performance Supercapacitor Application. *J. Colloid Interface Sci.* **2022**, *623*, 845−855.

(67) Patil, S.; Raut, S.; Pandit, B.; Pandey, S.; Pande, S. A.; Sankapal, B. Web-Analogues One-Dimensional Iron Hydroxide@ Cadmium Hydroxide Nanostructure: Electrochemical Supercapacitor. *J. Mater. Sci.: Mater. Electron.* **2021**, *32* (17), 22472−22480.

(68) Li, X.; Zhang, C.; Xin, S.; Yang, Z.; Li, Y.; Zhang, D.; Yao, P. Facile Synthesis of MoS2/Reduced Graphene Oxide@ Polyaniline for High-Performance Supercapacitors. *ACS Appl. Mater. Interfaces* **2016**, *8* (33), 21373−21380.

(69) Jian, X.; Li, H.; Li, H.; Li, Y.; Shang, Y. Flexible and Freestanding MoS2/RGO/CNT Hybrid Fibers for High-Capacity All-Solid Supercapacitors. *Carbon* **2021**, *172*, 132−137.

(70) Jiang, Q.; Shang, Y.; Sun, Y.; Yang, Y.; Hou, S.; Zhang, Y.; Xu, J.; Cao, A. Flexible and Multi-Form Solid-State Supercapacitors Based on Polyaniline/Graphene Oxide/CNT Composite Films and Fibers. *Diamond Relat. Mater.* **2019**, *92*, 198−207.

(71) Thakur, A. K.; Majumder, M.; Choudhary, R. B.; Singh, S. B. MoS2 Flakes Integrated with Boron and Nitrogen-Doped Carbon: Striking Gravimetric and Volumetric Capacitive Performance for Supercapacitor Applications. *J. Power Sources* **2018**, *402*, 163−173.